Characterizing output beams for lasers that use high-magnification unstable resonators

Saiedeh Saghafi, Michael J. Withford, and James A. Piper

Department of Physics, Macquarie University, Sydney NSW 2109, Australia

Received October 3, 2000; revised manuscript received December 21, 2000; accepted January 12, 2001

Laser beams generated from high-magnification on-axis unstable resonators by use of hard-edged optics typically have a doughnut-shaped distribution in the near field (i.e., a flat-top profile with a hole in the middle for an axially coupled beam). We derive analytical expressions describing this distribution by using the flattened Gaussian beams concept. The superposition of two flattened Gaussian beams whose flatness and steepness of edges are controlled by defined parameters (i.e., the beam width and the order) is used to analyze the output beam intensity along the propagation axis. Finally, experimental measurements of beam propagation from a copper-vapor laser fitted with a high-magnification unstable resonator show excellent agreement with theoretical predictions.

OCIS codes: 140.3460, 140.4780.

1. INTRODUCTION

The needs of many high-power visible laser applications (e.g., micromachining) are best met with laser sources that have both flat-top intensity profiles (a uniform energy density over a given cross section) and high beam quality (low-divergence output). However, developing lasers with both of these output characteristics can be technically challenging.

Many techniques have been used to improve the uniform laser beam. Optical elements can be employed both intracavity and extracavity to modify the spatial output characteristics of different lasers. Using specialized lenses to convert a Gaussian into a uniform beam profile,[1] applying tapered reflectivity mirrors to produce a flat-top profile in a solid-state laser,[2] using super-Gaussian unstable resonators in a laser with short-pulse high-gain active media,[3] and using graded-phase-mirror resonators in a cw CO_2 laser that produce a super-Gaussian output[4] are examples of these methods. A kinoform that shapes a Gaussian beam into a rectangular beam for semiconductor lasers is a further example of these methods.[5] High-aperture, high-gain systems can also produce spatially uniform output power when they employ conventional unstable-resonator geometries.[6] In these cases beam uniformity is obtained by the manipulation of the spatial gain characteristics by, for example, preionization of excimer lasers, alteration of the buffer-gas composition of copper-vapor lasers (CVL's), or alteration of the pump modes of diode-pumped solid-state lasers. These systems are widely used at the present time, and it is important for the output of these devices to be characterized analytically.

In the past most models used paraxial approximations to analyze uniform irradiance distributions[2,7,8]; these models effectively predict the beam's intensity profile, phase, spot size, and shape at any point along the propagation axis. In 1994, Gori[7] introduced a new analytical expression, the so-called flattened Gaussian beam (FGB), which can change from a general Gaussian to a flat-top beam by a change in the number of beam orders in a finite sum of Laguerre–Gaussian functions used in the expression. Sheppard *et al.*[8] introduced a different type of FGB that is defined at the waist to be the two-dimensional Fourier transform of the product of an Airy disk and a Gaussian. Another commonly used model for flattened beams is the super-Gaussian beam profile,[2] which also varies from a Gaussian beam to a flat-top beam as the number of the beam order increases.

Previous research in this area has been restricted to the modeling of relatively simple irradiance distributions: those varying from Gaussian to flat-top distributions. However, some high-average-power, high-beam-quality laser sources use unstable-resonator configurations that result in relatively complex output intensity profiles. For example, CVL's that use (positive-branch) on-axis unstable resonators and injection-seeded CVL oscillators have output intensity profiles that approximate a flat-top distribution with an axial shadow.[9] In this paper, we present details, based on the concept of FGB's developed by Gori,[7] of a model that not only describes Gaussians and FGB's but also describes flat-top beams with central shadows. The validity of this model is tested against the output of a CVL operating with an on-axis unstable resonator.

The beam quality and the flatness of the output of the CVL is also characterized by use of standard parameters. Although M^2 is the industry standard defining laser-beam quality, many researchers still use the times-diffraction-limited approach when quantifying the beam quality of lasers with flat-top irradiance distributions because of the perception that M^2 is mostly applicable to lasers with Gaussian and Gaussian-like irradiance distributions. In this paper, we show that the beam-propagation factor M^2 is reliable in quantifying the beam quality of lasers with flat-top distributions when the kurtosis parameter k, which provides useful information about beam shape, is also taken into consideration.

0740-3232/2001/071634-10$15.00

2. THEORY

A. Flattened Gaussian Beams

A new type of axially symmetric beams, termed FGB's, was introduced by Gori[7] in 1994. These beams were expressed as a finite sum of Laguerre–Gaussian functions. At the waist the beam can be described by

$$\psi = A\sum_{n=0}^{N} C_n L_n\left(\frac{2Nr^2}{w_0^2}\right)\exp\left(\frac{-N}{w_0^2}r^2\right), \qquad N = 1, 2, 3,\ldots, \tag{1}$$

where N is the number of beam orders,

$$C_n^N = (-1)^n \sum_{m=n}^{N}\binom{m}{n}\frac{1}{2^m}, \tag{2}$$

A is a constant, w_0 is the beam's spot size at the waist, and L_n is the Laguerre polynomial of the order n. The propagation of the Laguerre–Gaussian function, which compared higher-order Gaussian beam modes in cylindrical coordinates, was given by Siegman.[6] The beam distribution at a distance z from the waist plane for a field described by Eq. (1) can be obtained and takes the form

$$\psi_N(r,z) \approx \frac{w_N(0)}{w_N(z)}\exp\left\{i\left[kz - \Phi_N(z) + \frac{k}{2R_N(z)}\right]\right\} \times \exp\left[-\frac{r^2}{w_N^2(z)}\right]\sum_{n=0}^{N} C_n^N L_n\left[\frac{2r^2}{w_N^2(z)}\right] \times \exp[-2in\Phi_N(z)], \tag{3}$$

where k is the wave number, $w_N(z)$ is the beam spot size at z, $R_N(z)$ is the radius of the curvature, and $\phi_N(z)$ is the phase shift, formulated as

$$k = \frac{2\pi}{\lambda}, \tag{4}$$

$$w_N(z) = w_N(0)\left\{1 + \left[\frac{\lambda z}{\pi w_N^2(0)}\right]^2\right\}^{1/2}, \tag{5}$$

$$R_N(z) = z\left\{1 + \left[\frac{\pi w_N^2(0)}{\lambda z}\right]^2\right\}, \tag{6}$$

$$\Phi_N(z) = \arctan\left[\frac{\lambda z}{\pi w_N^2(0)}\right]. \tag{7}$$

The term $w_N(0)$ represents the spot size of the Laguerre–Gaussian function at $z = 0$, which is related to the width of the FGB's through

$$w_N(0) = \frac{w_0}{\sqrt{N}}. \tag{8}$$

B. Flattened Gaussian Beams with Central Shadows

The output of lasers operating with on-axis, high-magnification unstable resonators that use hard-edged optics typically have doughnut-shaped near-field intensity distributions. In this paper the propagation of these types of unstable resonators is investigated by use of the FGB concept. The superposition of a constructed FGB

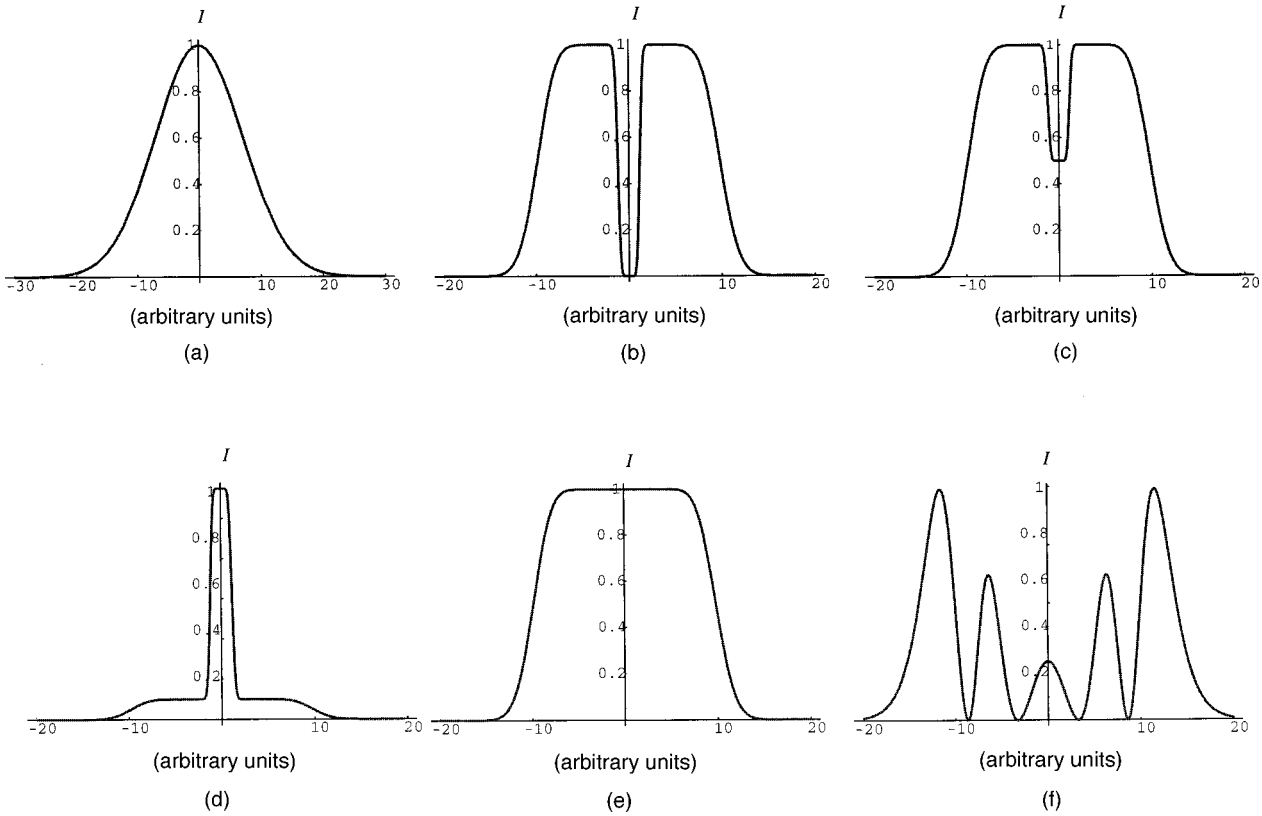

Fig. 1. Different beam profiles obtained by use of Eq. (13): (a) $\eta = 0$ and $N = 0$; (b) $\eta = 1$, $N = 9$, $B = 5$, and $\epsilon = 0.12$; (c) $\eta = 0.5$, $N = 9$, $B = 5$, and $\epsilon = 0.12$; (d) $\eta = -10$, $N = 9$, $B = 5$, and $\epsilon = 0.12$; (e) $\eta = 0$ and $N = 9$; (f) $\eta = 0.9$, $N = 0$, $B = 5$, and $\epsilon = 0.12$.

and the one described by Eq. (1) gives an expression for a FGB with a hole in the middle (FGBHM). At the waist the second FGB, which varies in the amplitude distribution and the steepness from Eq. (1), is written as

$$\psi_{B0} = A\sum_{n=0}^{B} C_n^B L_n\left(\frac{2Br^2}{\nu_0^2}\right)\exp\left(-\frac{Br^2}{\nu_0^2}\right),$$

$$B = 1, 2, 3, \ldots, \tag{9}$$

where

$$C_n^B = (-1)^n \sum_{m=n}^{B} \binom{m}{n}\frac{1}{2^m}. \tag{10}$$

The spot size of this beam is related to the spot size of the first FGB through a variant parameter ϵ that controls the diameter of the hole in $\nu_0 = \epsilon w_0$.

An expression similar to expression (3) is obtained to describe the propagation of the second FGB

$$\psi_B(r,z) \approx \frac{\nu_B(0)}{\nu_B(z)}\exp\left\{i\left[kz - \Phi_B(z) + \frac{k}{2R_B(z)}\right]\right\} \times \exp\left[-\frac{r^2}{\nu_B^2(z)}\right]\sum_{n=0}^{B} C_n^B L_n\left[\frac{2r^2}{\nu_B^2(z)}\right] \times \exp[-2in\Phi_B(z)], \tag{11}$$

where one can formulate $\nu_B(z)$, $R_B(z)$, and $\phi_B(z)$ by replacing $w(z)$ with $\nu(z)$ and changing the subscript N to B. The spot size of the Laguerre–Gaussian function, $\nu_B(0)$, is related to the width of the FGB through

$$\nu_B(0) = \frac{\nu_0}{\sqrt{B}}. \tag{12}$$

Then the superposition of these FGB's provides the formula

$$\psi_{ur}(r,z) = \psi_N(r,z) - \eta\psi_B(r,z), \tag{13}$$

where B, the beam order of the constructed FGB, controls the steepness of the shoulders of the hole and η is a variable constant whereby various spatial intensity distributions can be achieved by one's changing η. For example, $\eta = 0$ describes general Gaussian distributions when $B = N = 0$ and FGB's when $B = 0$ and $N \neq 0$, whereas $\eta = 1$ describes FGBHM's (see Fig. 1). The wide range of application of Eq. (13) can be illustrated by Fig. 1. In fact, Eq. (13) can predict the irradiance distribution created by finite-mirror stable resonators [see Fig. 1(c)].

The intensity profile can be derived with

$$I_{ur}(r,z) = [\psi_N(r,z) - \eta\psi_B(r,z)] \times [\psi_N(r,z) - \eta\psi_B(r,z)]^* = I_N(r,z) + I_B(r,z) + I_p(r,z), \tag{14}$$

where

$$I_N(r,z) = \psi_N(r,z)\psi_N^*(r,z) = \frac{w_N^2(0)}{w_N^2(z)}\exp\left[-\frac{2r^2}{w_N^2(z)}\right] \times \left(\left\{\sum_{n=0}^{N} C_n^N L_n\left[\frac{2r^2}{w_N^2(z)}\right]\cos[2n\Phi_N(z)]\right\}^2 + \left\{\sum_{n=0}^{N} C_n^N L_n\left[\frac{2r^2}{w_N^2(z)}\right]\sin[2n\Phi_N(z)]\right\}^2\right), \tag{15}$$

$$I_B(r,z) = \eta^2|\psi_B(r,z)\psi_B^*(r,z)| = \eta^2\frac{\nu_B^2(0)}{\nu_B^2(z)}\exp\left[-\frac{2r^2}{\nu_B^2(z)}\right] \times \left(\left\{\sum_{n=0}^{B} C_n^B L_n\left[\frac{2r^2}{\nu_B^2(z)}\right]\cos[2n\Phi_B(z)]\right\}^2 + \left\{\sum_{n=0}^{B} C_n^B L_n\left[\frac{2r^2}{\nu_B^2(z)}\right]\sin[2n\Phi_B(z)]\right\}^2\right). \tag{16}$$

By use of expressions (3) and (11) I_p can be formulated as

$$\begin{aligned} I_p(r,z) = {} & \eta\frac{w_N(0)}{w_N(z)}\frac{\nu_B(0)}{\nu_B(z)}\exp\left\{-\left[\frac{1}{w_N^2(z)} + \frac{1}{\nu_B^2(z)}\right]r^2\right\} \\ & \times 2\left(\left\{\sum_{n=0}^{N} C_n^N L_n\left[\frac{2r^2}{w_N^2(z)}\right]\cos[2n\Phi_N(z)]\right\} \times \left\{\sum_{n=0}^{B} C_n^B L_n\left[\frac{2r^2}{\nu_B^2(z)}\right]\cos[2n\Phi_B(z)]\right\} \right. \\ & \left. + \left\{\sum_{n=0}^{N} C_n^N L_n\left[\frac{2r^2}{w_N^2(z)}\right]\sin[2n\Phi_N(z)]\right\} \times \left\{\sum_{n=0}^{B} C_n^B L_n\left[\frac{2r^2}{\nu_B^2(z)}\right]\sin[2n\Phi_B(z)]\right\}\right) \\ & \times \cos\left[-\Phi_N(z) + \Phi_B(z) + \frac{k}{2R_N(z)} - \frac{k}{2R_B(z)}\right] \\ & - 2\left(\left\{\sum_{n=0}^{N} C_n^N L_n\left[\frac{2r^2}{w_N^2(z)}\right]\cos[2n\Phi_N(z)]\right\} \times \left\{\sum_{n=0}^{B} C_n^B L_n\left[\frac{2r^2}{\nu_B^2(z)}\right]\sin[2n\Phi_B(z)]\right\} \right. \\ & \left. - \left\{\sum_{n=0}^{N} C_n^N L_n\left[\frac{2r^2}{w_N^2(z)}\right]\sin[2n\Phi_N(z)]\right\} \times \left\{\sum_{n=0}^{B} C_n^B L_n\left[\frac{2r^2}{\nu_B^2(z)}\right]\cos[2n\Phi_B(z)]\right\}\right) \\ & \times \sin\left[-\Phi_N(z) + \Phi_B(z) + \frac{k}{2R_N(z)} - \frac{k}{2R_B(z)}\right]. \end{aligned} \tag{17}$$

Finally, by substituting Eqs. (15)–(17) into Eq. (14), we can predict the beam-profile distribution at various points along the propagation axis.

C. Beam-Propagation Factor M^2 and the Kurtosis Parameter k

The beam-propagation factor and the kurtosis parameter are commonly used in the study of optical systems. These two parameters are able to quantify beam quality and flatness. In this paper these two parameters are used to complete the characterization of the FGBHM. M^2 and k can be defined in both cylindrical and rectangular coordinates. If the complex field amplitude at the waist of a symmetrical beam is written as $\psi(r, 0)$, the beam-propagation factor, by use of the far-field or the near-field distribution, is defined as[10]

$$M^2 = \frac{\left\{\left[\int_0^\infty \left|\psi(r,0)\right|^2 r^2 \mathrm{d}r\right]\left[\int_0^\infty \left|\frac{\mathrm{d}\psi(r,0)}{\mathrm{d}r}\right|^2 \mathrm{d}r\right]\right\}^{1/2}}{\int_0^\infty |\psi(r,0)|^2 \mathrm{d}r}. \tag{18}$$

Kurtosis is used to quantify a beam's flatness (or sharpness) compared with normal Gaussian beams.[11] As a standard parameter it provides a single number that reveals useful information about the shape of the beam (i.e., $k = 3$ at the waist, indicating a Gaussian output, $k > 3$ belonging to a group of beams whose intensity beam profiles are sharper than that of a Gaussian beam, and $k < 3$ defining beams flatter than a Gaussian beam). It can be expressed in terms of the second and the fourth moments of the normalized field:

$$k = \frac{\left[\int_0^\infty \left|\psi(r,z)\right|^2 r^4 \mathrm{d}r\right]\left[\int_0^\infty \left|\psi(r,z)\right|^2 \mathrm{d}r\right]}{\left[\int_0^\infty \left|\psi(r,z)\right|^2 r^2 \mathrm{d}r\right]^2}. \tag{19}$$

3. EXPERIMENT

A. Experimental Method

The laser used in this study was a conventional CVL [active volume, 25 mm (diameter) × 1 m (long)] with a thyratron-switched, single-stage pulse-compression excitation circuit. The laser was operated with a 2% H_2–Ne buffer gas (buffer-gas pressure, 40 Torr) at a pulse-repetition frequency of 10 kHz. The optical resonator used was an on-axis positive-branch confocal unstable resonator of magnification $M = 100$ that incorporated a concave 4-m-high reflector and a convex 40-mm radius of curvature hard-edged spot reflector with a diameter of 2 mm. Note that the spot reflector is mounted on a glass stalk that is set at a small angle to the propagation axis. As a result, the shadow of the spot reflector is slightly larger than 2 mm in diameter (2.4 mm; see Fig. 2).

For the purposes of this study the laser was operated at a relatively low input power corresponding to a total output power of 3.8 W: 3.2 W of green (511-nm) and 0.6 W of yellow (578-nm) output. It is important to note that the CVL's output is pulsed (typical duration, 40–50 ns) and consists of three main components that result from the stepwise evolution of the beam quality with this type of optical cavity,[12] namely, highly divergent amplified spontaneous emission that has undergone fewer than two round trips in the resonator cavity and in this experiment is negligible, low-divergent output corresponding to radiation having undergone two round trips, and, finally, near-diffraction-limited output undergoing three or more round trips. It should be stated that the second two of the three temporal components of the output beam create a coherent beam.[13]

Pulse-averaged near-field intensity profiles of the green component of the laser output were recorded by use of a dichroic filter to reject the yellow component and the imaging, by means of an $f = 250$ mm achromatic lens, onto the CCD camera (Spiricon, Model TM 745) of a laser beam analyzer (Spiricon, Model LBA-PC). After optimization by use of the knife-edge method this imaging configuration was fixed to an optical rail to ensure self-consistency as near-field intensity profiles were recorded at different positions along the propagation axis, namely, $z = 0$, 0.85, 2.45, 5.05, 15.3 m; $z = 0$ corresponds to the plane immediately behind the output coupler.

We examined the pulse-averaged far-field intensity profiles of the green laser output by taking a low-power sample of the output (by means of reflections from several wedges) and then bringing this sample to focus with an $f = 450$ mm achromatic doublet. A magnified image of this focal spot was produced on the CCD camera of the laser-beam analyzer by use of an $f = 75$ mm singlet (the imaging distance was 2.4 m).

B. Experimental Results

Intensity profiles of the near field at different positions (i.e., $z = 0$, 0.85, 2.45, 5.05, 15.3 m) along the propagation axis were measured; sample data are shown in Figs. 3–8. The near-field intensity profile at $z = 0$ (the plane of first measurements of the wave front, i.e., the waist directly in front of the CVL) is a top hat with a central shadow caused by the on-axis spot reflector used in the laser resonator. At $z = 0.85$ m (85 cm from the first plane of measurement, $z = 0$), the shoulders of the near-field intensity profile are rounded, and a Poisson spot is evident in the center of the shadow. The shoulders of the near-field intensity profiles become increasingly rounded and the spot reflector shadow less distinct as the distance z increases toward the far field.

In the far field the intensity profile is dominated by a central (diffraction-limited) peak corresponding to a more than three round-trip output that sits atop a small shoul-

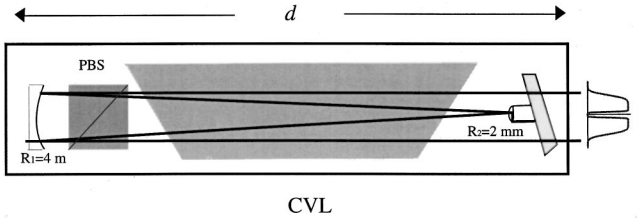

Fig. 2. High-magnification CVL unstable resonator. PBS, polarizing beam splitter.

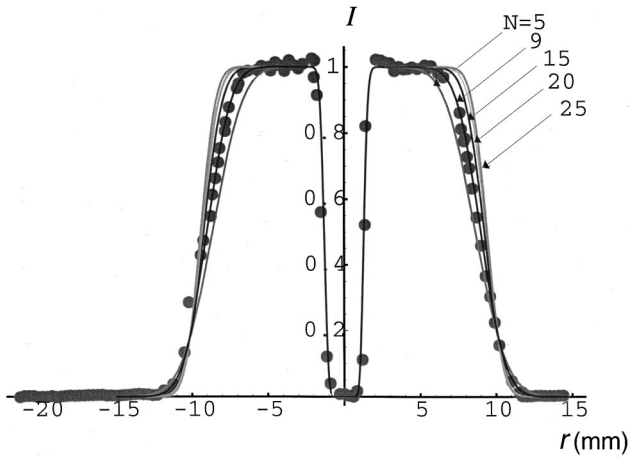

Fig. 3. Definitions for B, N, and ϵ and comparison of the theoretical results (solid curves) with the measured data (circles) at $z = 0$.

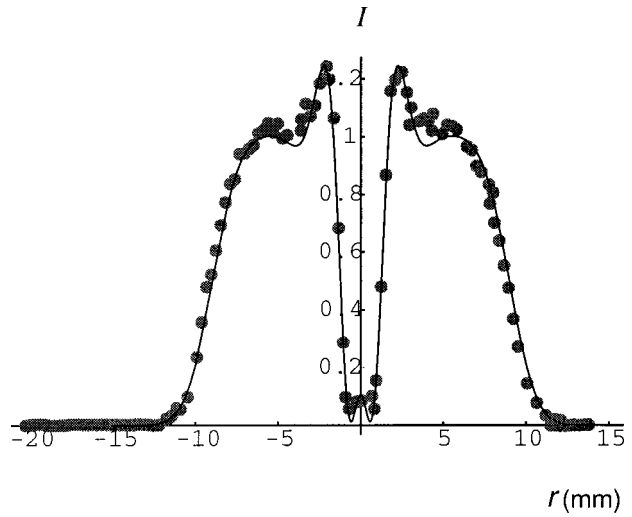

Fig. 4. Agreement between the theoretical results (solid curves) and the measured data (circles) at $z = 85$ cm.

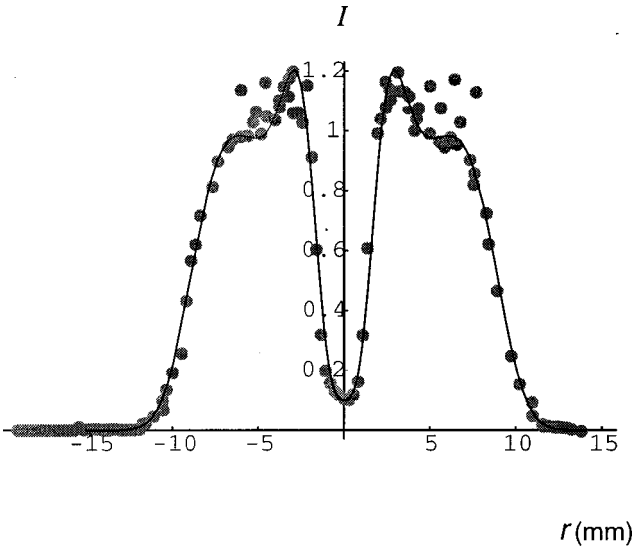

Fig. 5. Agreement between the theoretical results (solid curves) and the measured data (circles) at $z = 245$ cm.

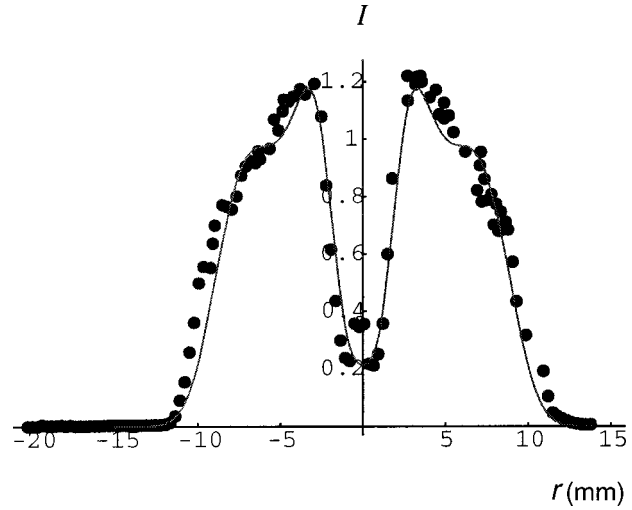

Fig. 6. Agreement between the theoretical results (solid curves) and the measured data (circles) at $z = 505$ cm.

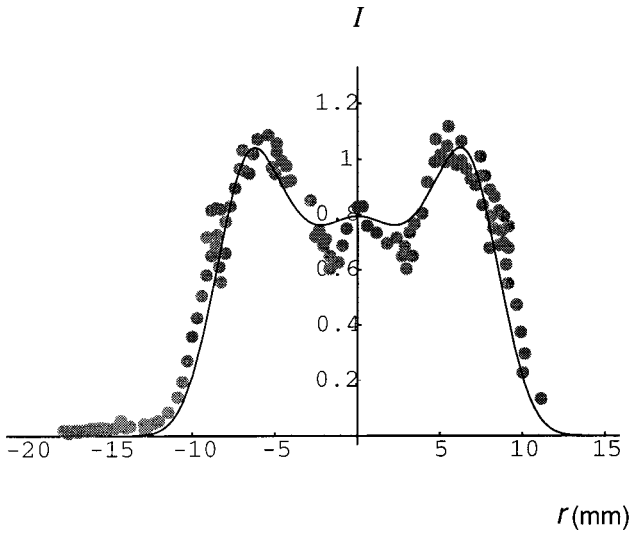

Fig. 7. Agreement between the theoretical results (solid curves) and the measured data (circles) at $z = 15{,}300$ cm.

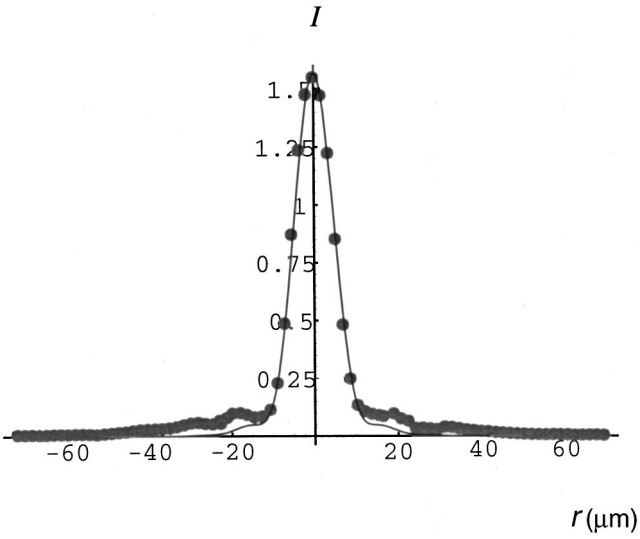

Fig. 8. Agreement between the theoretical results (solid curves) and the measured data (circles) at the far field.

der that arises from the low-divergence, two round-trip output component. Both of these components overlay a highly divergent amplified spontaneous emission layer, which is not discernible at this scale.

C. Analytical Results

Generally, the usefulness of a model is established from the parallels between its analytical and experimental results. In Subsection 3.B a mathematical expression and its elements were discussed.

The theoretical expression for the beam intensity profile at $z = 0$ and where $\eta = 1$ can be obtained by use of Eqs. (1), (9), and (13):

$$I_0 = |\psi_{N0} - \psi_{B0}|^2$$

$$\approx \left[\sum_{n=0}^{N} C_n^N L_n\left(\frac{2Nr^2}{w_0^2}\right) \exp\left(\frac{-N}{w_0^2} r^2\right) - \sum_{n=0}^{B} C_n^B L_n\left(\frac{2Br^2}{\nu_0^2}\right) \exp\left[-\frac{Br^2}{\nu_0^2}\right] \right]^2. \quad (20)$$

The parameter ϵ in expression (20) was fixed at 0.12 to create a flat-top intensity profile that was recorded at $z = 0$ with a central shadow (2.4 mm) compared with the overall beam width of $w_0 = 24$ mm. The values of N and B were varied in expression (20) to give the best fit to the near-field intensity profile measured at the exit plane of the laser ($z = 0$). The best fit between the analytical and the experimental results corresponded to values of N and B of 9 and 5, respectively.

Using the theory of the second moment [Eq. (18)], we are able to obtain the theoretical values of the beam-propagation factor for different beam orders M_T^2. For systems that use a lens of focal length f to image the far field a useful equation used by experimentalists to derive the beam-propagation factor[14] is

$$M_{\text{exp}}^2 = \frac{4\pi d_0 D_0}{\lambda f}, \quad (21)$$

where d_0 and D_0 are the diameters of the beam in the near and the far fields, respectively. However, the full angle of divergence in the paraxial regime is given by[14]

$$\theta = \frac{4\lambda M^2}{\pi d_0}, \quad (22)$$

where M^2 is the beam-propagation factor. Thus by replacing M^2 in Eq. (22) with M_T^2 or M_{exp}^2, we are able to predict the full angle of divergence in two regimes. The extension of the beam-divergence angle beyond the angle predicted by theory is expressed by β (see Fig. 13, below). Thus in the experimental regime the full angle of divergence is described by $\alpha + \beta$, where $\alpha = 4\lambda M_T^2/\pi d_0$. It should be mentioned that α and β are both effectively small. Because the real beam from the test laser is imperfect (having two-pass or even three-pass beams with angles of divergence larger than the one predicted theoretically), obtaining a tool that enables us to estimate the beam intensity distribution at an arbitrary plane is necessary.

Such a tool can be realized by use of a constructed z instead of a real z (z_{exp}). Because of the higher angle of divergence in the experiment, the beam spot size at any arbitrary plane of measurement is bigger than the one predicted by theory. However, geometrical optics enables us to find the relation between z_{exp} and the constructed z, which provides a similar spot size. This relation is considered as a scaling formula and is derived in detail in Appendix A. It is shown that the constructed z and z_{exp} are related through α and β (i.e., $\beta = \theta - \alpha$). These two angles can be calculated by use of M_T^2 (the theoretical value of the beam-propagation factor), M_{exp}^2 (the experimental beam-propagation factor), and Eq. (22).

Therefore, as was stated above, measuring the beam intensity profile in the near and the far fields and comparing it with the theoretical distribution allows parameters such as N and B to be determined. Using our scaling equations in Appendix A, we can calculate the constructed z for any plane of measurement (at z_{exp}); hence Eq. (14) predicts the intensity profile at any plane (see Figs. 4–8).

5. DISCUSSION

The analytically predicted near-field intensity profiles (at $z = 2.45, 5.05, 15.3$ m) and the measured far-field intensity profile show excellent agreement with the experimentally measured derived results (Figs. 4–8). There is also good agreement between the beam-propagation factors M^2 obtained in the two regimes. In particular, the measured M^2 of 2.575 that was determined with the $D86\%$ method and Eq. (21) compares very well with the value of M^2 of 2.41 that was derived from Eqs. (13) and (18), i.e., the second-moment method, when $N = 9$ and $B = 5$.

These analytical expressions have important implications for improving laser-beam quality by the manipulation of the laser spatial gain characteristics. For example, Fig. 9 shows the beam-propagation factor for fixed values of B, ϵ, and η (i.e., 5, 0.12, and 1, respectively) plotted against the beam order N. As N increases the computed values of M^2 reach a minimum at $N = B$ and then increase (Fig. 9). An intensity profile at $N = B$ has a spatial distribution with a better beam-propagation factor than the one produced by the CVL used in this study (corresponding to beam orders of $N = 9$ and $B = 5$). The axial output intensity profile of these lasers can readily be tailored by the addition of trace concentrations of hydrogen.[15]

The analytical expressions presented in this paper also have important implications for the design and the optimization of laser resonator configurations and for matching these to specific applications. For example, the effect of the size of the output-coupler shadow on M^2 for fixed values of N, B, and η (i.e., 9, 5, and 1, respectively) is shown in Fig. 10. These results show that, for this beam profile, the beam quality will be higher if the diameter of

the shadow is increased. Although some loss in the total output power may result, for many applications this trade-off between output power and high beam quality will be acceptable.

As was mentioned in Section 2, CVL unstable resonators are capable of producing either FGB's or FGBHM's by use of different cavities. The analytical expression for the kurtosis parameter of a FGB ($\eta = 0$) at the waist ($z = 0$) is derived as[16]

$$K_{\mathrm{FGB}} = \frac{9}{5}\frac{\Gamma\left(2N+\frac{9}{2}\right)\Gamma\left(2N+\frac{5}{2}\right)\left(N+\frac{5}{2}\right)^2 F\left(1, 2N+\frac{9}{2}; N+\frac{9}{2}; \frac{1}{2}\right)F\left(1, 2N+\frac{5}{2}; N+\frac{5}{2}; \frac{1}{2}\right)}{\Gamma\left(2N+\frac{7}{2}\right)^2\left(N+\frac{3}{2}\right)\left(N+\frac{7}{2}\right)\left[F\left(1, 2N+\frac{7}{2}; N+\frac{7}{2}; \frac{1}{2}\right)\right]^2}. \quad (23)$$

It can be seen the asymptotic value for the kurtosis parameter of FGB's is 1.8 (in rectangular coordinates). It can be concluded that, as the degree of flatness for an irradiance distribution increases, the value of k changes from 3 (perfect Gaussian) toward 1.8 (rectangular function).[17] Here at $z = 0$, for fixed values of N (i.e., 5, 20, and 40) the numerical value of the kurtosis parameter of a FGBHM ($\eta = 1$), by use of Eqs. (13) and (21), is calculated and its changes versus ϵ are plotted in Fig. 11.

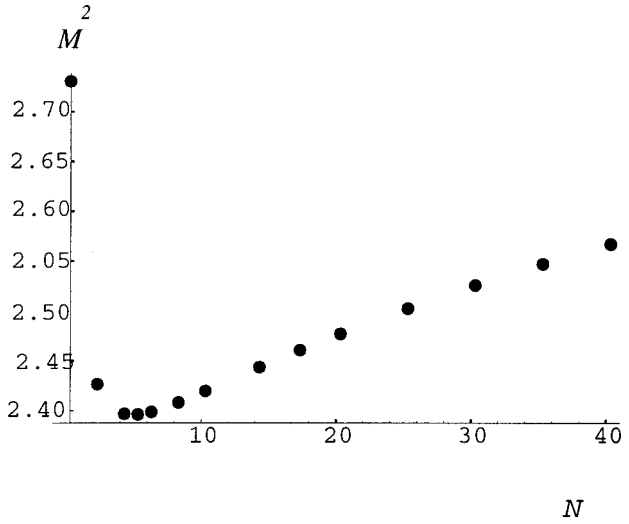

Fig. 9. Changes of M^2 versus N for $B = 5$, $\eta = 1$, and $\epsilon = 0.12$.

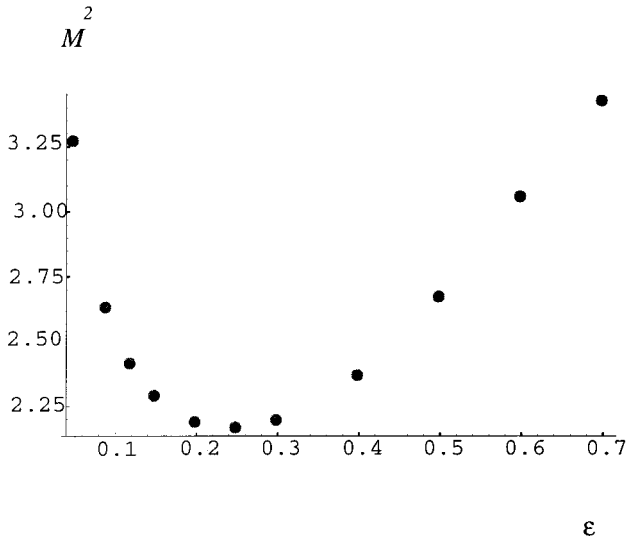

Fig. 10. Changes of M^2 versus ϵ for $N = 9$, $B = 5$, and $\eta = 1$.

To reveal more information about the flatness of the FGBHM and to compare it with the FGB requires that the changes of k versus the beam order N for fixed values of ϵ be obtained. The comparison between values of the

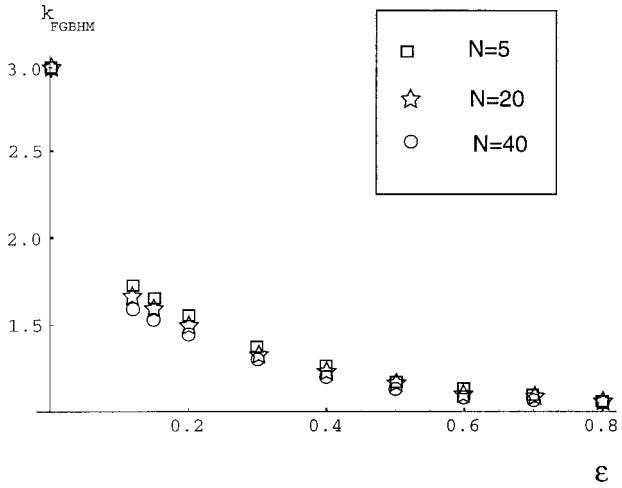

Fig. 11. Changes of k versus ϵ for $N = 5, 20, 40$.

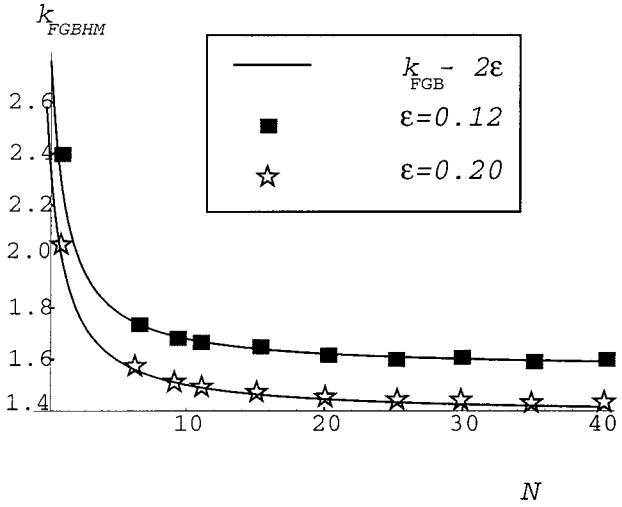

Fig. 12. Changes of k for the FGBHM versus N for $\epsilon = 0.12, 0.2$.

kurtosis parameters for FGB's [i.e., Eq. (23)] and for FGBHM's (numerical values for the same beam order) leads us toward

$$k_{\mathrm{FGBHM}} = k_{\mathrm{FGB}} - 2\epsilon. \tag{24}$$

Equation (24) for two values of ϵ is plotted in Fig. 12.

We are thus able to use our data that are related to a FGB and the laser parameters to design a new cavity that produces a desirable FGBHM (by changing the size of the small reflector R_2) and to predict the shape of the field distribution for different beam orders. It must be noted that ϵ is a parameter without units; however, 20ϵ approximates the dimensionless value of the size of shadow.

Comparing the computed results with the experimental data aids in developing methods for removing unwanted effects, such as diffraction, aberrations, and so forth, and leads to improvement of the optical systems. The kurtosis parameter in the far field can also reveal useful information about the sharpness of the beam in the far field that is crucial for microdrilling.

6. SUMMARY AND CONCLUSION

We have proposed a beam-propagation model that is applicable to lasers that produce Gaussian beams, flat-top beams, and flat-top beams with a hole in the middle. Comparison between the experimental data and the theoretical results shows good agreement between experiment and theory. A number of extensions to the model could be considered. For example, the model can be used to characterize the output beam produced by Nd:YAG unstable resonators that use a Gaussian reflectivity mirror in the cavity ($B = 0$ and $\eta = 1$). The model can also be used to predict the exact far-field plane for real laser sources that are used for high-pressure laser micromachining. Equations (18) and (19) have the advantage of providing a single number with which to analyze the beam spot size and shape. Equations (23) and (24) can be used to reorganize the optical setup inside the cavity to produce a desirable FGBHM from a related FGB. We are currently extending the present approach to investigate a laser beam with off-axis shadows (edge-coupled injection-seeded systems) and asymmetric beams (CO_2 waveguide arrays, diode arrays, etc).

APPENDIX A

A scaling formula for z_{exp} is obtained by use of geometrical optics tools. By replacing the scaled z, z_T, in Eq. (14), one can predict the beam intensity even when it goes beyond the paraxial approximation. Figure 13 shows the beam propagation along the z axis. It can be seen that

$$\tan\left(\frac{\alpha}{2}\right) = \frac{AB}{2z_0} = \frac{AB + 2\delta_2}{2(z_0 + z_{\mathrm{exp}})} = \frac{AB + 2\delta_1}{2(z_0 + z_T)} = \frac{\delta_2}{z_{\mathrm{exp}}} = \frac{\delta_1}{z_T}, \tag{A1}$$

where $\alpha/2$ is the semiangle of divergence in the paraxial regime and AB is the diameter of the aperture.

The beam diameter at z_{exp} (in the experimental case) is

$$w_{\mathrm{exp}} = CD = AB + 2\delta_1 = AB + 2z_{\mathrm{exp}}\tan\left(\frac{\alpha + \beta}{2}\right), \tag{A2}$$

where $(\alpha + \beta)/2$ is the semiangle of divergence beyond the paraxial approximation. An identical beam diameter to the one described by Eq. (2) can be realized in the paraxial approximation at z_T:

$$w_{\mathrm{exp}} = EF = AB + 2\delta_1 = AB + 2z_T\tan\left(\frac{\alpha}{2}\right). \tag{A3}$$

From Eq. (A1) it can be seen that

$$z_T = \frac{AB + 2\delta_1}{AB + 2\delta_2}(z_0 + z_{\mathrm{exp}}) - z_0 \tag{A4}$$

and that z_0 is given by $(AB)/2\tan(\alpha/2)$; therefore Eq. (A4) changes to

$$z_T = \frac{AB + 2z_{\mathrm{exp}}\tan\left(\frac{\alpha + \beta}{2}\right)}{AB + 2z_{\mathrm{exp}}\tan\left(\frac{\alpha}{2}\right)}\left[\frac{AB}{2\tan\left(\frac{\alpha}{2}\right)} + z_{\mathrm{exp}}\right] - \frac{AB}{2\tan\left(\frac{\alpha}{2}\right)}. \tag{A5}$$

Equation (5) can be simplified by use of

$$\tan\left(\frac{\alpha + \beta}{2}\right) = \frac{\tan\left(\frac{\alpha}{2}\right) + \tan\left(\frac{\beta}{2}\right)}{1 - \tan\left(\frac{\alpha}{2}\right)\tan\left(\frac{\beta}{2}\right)}$$

as

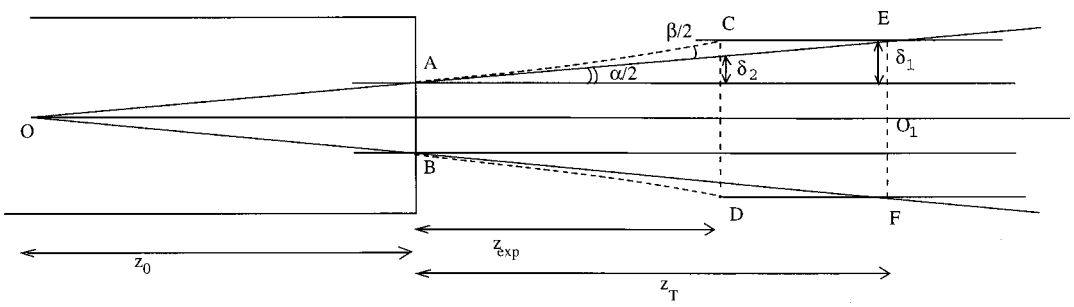

Fig. 13. Propagation of the beam in and beyond the paraxial approximation regime.

$$z_T = \frac{AB}{2\tan\left(\frac{\alpha}{2}\right)} \times \left\{ \frac{AB + 2z_{\exp}\left[\frac{\tan\left(\frac{\alpha}{2}\right) + \tan\left(\frac{\beta}{2}\right)}{1 - \tan\left(\frac{\alpha}{2}\right)\tan\left(\frac{\beta}{2}\right)}\right]}{AB + 2z_{\exp}\tan\left(\frac{\alpha}{2}\right)} - 1 \right\} + \frac{AB + 2z_{\exp}\left[\frac{\tan\left(\frac{\alpha}{2}\right) + \tan\left(\frac{\beta}{2}\right)}{1 - \tan\left(\frac{\alpha}{2}\right)\tan\left(\frac{\beta}{2}\right)}\right]}{AB + 2z_{\exp}\tan\left(\frac{\alpha}{2}\right)} z_{\exp}. \quad \text{(A6)}$$

Equation (A6) can be simplified as

$$z_T = \frac{AB}{2\tan\left(\frac{\alpha}{2}\right)} \left\{ \frac{2z_{\exp}\tan\left(\frac{\beta}{2}\right)\left[1 + \tan^2\left(\frac{\alpha}{2}\right)\right]}{\left[1 - \tan\left(\frac{\alpha}{2}\right)\tan\left(\frac{\beta}{2}\right)\right]\left[AB + 2z_{\exp}\tan\left(\frac{\alpha}{2}\right)\right]} \right\} + \frac{AB\left[1 - \tan\left(\frac{\alpha}{2}\right)\tan\left(\frac{\beta}{2}\right)\right] + 2z_{\exp}\left[\tan\left(\frac{\alpha}{2}\right) + \tan\left(\frac{\beta}{2}\right)\right]}{\left[1 - \tan\left(\frac{\alpha}{2}\right)\tan\left(\frac{\beta}{2}\right)\right]\left[AB + 2z_{\exp}\tan\left(\frac{\alpha}{2}\right)\right]} z_{\exp}$$

$$= \frac{z_{\exp}\left[\tan\left(\frac{\beta}{2}\right) + \tan\left(\frac{\alpha}{2}\right)\right] + \frac{2}{AB}z_{\exp}^2\tan\left(\frac{\alpha}{2}\right)\left[\tan\left(\frac{\alpha}{2}\right) + \tan\left(\frac{\beta}{2}\right)\right]}{\tan\left(\frac{\alpha}{2}\right)\left[1 - \tan\left(\frac{\alpha}{2}\right)\tan\left(\frac{\beta}{2}\right)\right]\left[1 + \frac{2}{AB}z_{\exp}\tan\left(\frac{\alpha}{2}\right)\right]}, \quad \text{(A7)}$$

where α and β are considered to be small; therefore $\tan(\alpha/2) = \alpha/2$ and $\tan(\beta/2) = \beta/2$. For $(\alpha/AB)z_{\exp} \ll 1$, we have

$$\frac{1}{\left(1 + \frac{\alpha}{AB}z_{\exp}\right)} \approx \left(1 - \frac{\alpha}{AB}z_{\exp}\right). \quad \text{(A8)}$$

By substituting expression (A8) into Eq. (A7), we can achieve a new scaling form for small $z_{\exp}$

$$z_T = Q\left\{\left(1 - \frac{\alpha}{AB}z_{\exp}\right) \times \left[z_{\exp}(\alpha + \beta) + \frac{\alpha}{AB}z_{\exp}^2(\alpha + \beta)\right]\right\} \approx Q\left[z_{\exp}(\alpha + \beta) - \frac{\alpha}{AB}z_{\exp}^2(\alpha + \beta)\right], \quad \text{(A9)}$$

where

$$Q = \frac{1}{\alpha\left(1 - \frac{\alpha\beta}{4}\right)}. \quad \text{(A10)}$$

However, for large values of $z_{\exp}$ the scaling formula obtains a more simplified format:

$$z_T = Q(\alpha + \beta)z_{\exp}. \quad \text{(A11)}$$

ACKNOWLEDGMENTS

The authors would like to thank Colin Sheppard for useful discussion about the FGB's concept and Jennifer Fishburn for helpful discussions about copper-vapor lasers. The authors also thank both the Centre of Lasers and Applications and Macquarie University.

REFERENCES

1. D. Shafer, "Gaussian to flat-top intensity distribution lens," Opt. Laser Technol. **14**, 159–160 (1982).
2. S. De Silvestri, P. Laporta, V. Magni, and O. Svelto, "Solid-state laser unstable resonators with tapered reflectivity mirrors: the super-Gaussian approach," IEEE J. Quantum Electron. **24**, 1172–1177 (1988).
3. M. R. Perrone, A. Piegari, and S. Scaglione, "On the super-

Gaussian unstable resonators for high-gain short-pulse laser media," IEEE J. Quantum Electron. **29**, 1423–1427 (1993).
4. R. V. Neste, C. Parè, R. L. Lachance, and P. A. Blanger, "Graded-phase mirror resonator with a super-Gaussian output in a cw CO_2 laser," IEEE J. Quantum Electron. **30**, 2663–2669 (1994).
5. J. Bengtsson, "A kinoform-only Gaussian-to-rectangle beam shaper for a semiconductor laser," Appl. Opt. **35**, 3807–3814 (1996).
6. A. E. Siegman, *Lasers* (University Science, Mill Valley, Calif., 1986).
7. F. Gori, "Flattened Gaussian beams," Opt. Commun. **107**, 335–341 (1994).
8. C. J. R. Sheppard and S. Saghafi, "Flattened light beams," Opt. Commun. **132**, 144–152 (1996).
9. J. J. Chang, "Time-resolved beam-quality characterization of copper-vapor lasers with unstable resonators," Appl. Opt. **33**, 2255–2265 (1994).
10. S. Saghafi and C. J. R. Sheppard, "The beam-propagation factor for higher-order Gaussian beams," Opt. Commun. **153**, 207–210 (1998).
11. R. Martínez-Herrera, G. Piquero, and P. M. Mejías, "On the propagation of the kurtosis parameter of general beams," Opt. Commun. **115**, 225–232 (1995).
12. D. W. Coutts, D. J. W. Brown, and J. A. Piper, "Measurements of the divergence evolution of a copper-vapor laser output by using a cylindrical imaging technique," Appl. Opt. **32**, 2058–2061 (1993).
13. D. W. Coutts, M. D. Ainsworth, and J. A. Piper, "Observation of the temporal evolution of transverse coherence in copper vapor lasers," Opt. Commun. **87**, 245–248 (1992).
14. T. F. Johnstone, Jr., "M^2 concept characterizes beam quality," Laser Focus World **May**, 173–183 (1990).
15. M. J. Withford, D. J. W. Brown, D. W. Coutts, and J. A. Piper, "Increased efficiency of high beam quality extraction from a vapor laser with H_2–Ne admixtures," IEEE J. Quantum Electron. **31**, 898–904 (1995).
16. S. Saghafi and G. W. Forbes have prepared the following paper for publication: "Defining the correspondence M^2 factor and k parameter for flat-top beams."
17. S. A. Amarande, "Beam propagation factor and the kurtosis parameter of flattened Gaussian beams," Opt. Commun. **129**, 311–315 (1996).